Separation of absorption and scattering profiles in spectroscopic optical coherence tomography using a least-squares algorithm

Chenyang Xu, Daniel L. Marks, Minh N. Do, and Stephen A. Boppart

Department of Electrical and Computer Engineering, Beckman Institute, University of Illinois at Urbana-Champaign, 405 N Mathews Ave., Urbana, IL 61801
boppart@uiuc.edu

Abstract: In spectroscopic optical coherence tomography, it is important and useful to separately estimate the absorption and the scattering properties of tissue. In this paper, we propose a least-squares fitting algorithm to separate absorption and scattering profiles when near-infrared absorbing dyes are used. The algorithm utilizes the broadband Ti:sapphire laser spectrum together with joint time-frequency analysis. Noise contribution to the final estimation was analyzed using simulation. The validity of our algorithm was demonstrated using both single-layer and multi-layer tissue phantoms.

OCIS codes: (170.4500) Optical coherence tomography; (300.1030) Absorption; (300.6360) Spectroscopy, Laser; (290.0290) Scattering; (290.7050) Turbid media.

References and links

1. D. Huang, E. A. Swanson, C. P. Lin, J. S. Schuman, W. G. Stinson, W. Chang, M. R. Hee, T. Flotte, K. Gregory, C. A. Puliafito and J. G. Fujimoto, "Optical coherence tomography," Science **254,** 1178-1181 (1991).
2. J. G. Fujimoto, M. E. Brezinski, G. J. Tearney, S. A. Boppart, B. E. Bouma, M. R. Hee, J. F. Southern and E. A. Swanson, "Biomedical imaging and optical biopsy using optical coherence tomography," Nature Medicine **1,** 970-972 (1995).
3. A. F. Fercher, W. Drexler, C. K. Hitzenberger and T. Lasser, "Optical coherence tomography - principles and applications," Rep. Prog. Phys, **66,** 239-303 (2003).
4. U. Morgner, W. Drexler, F. C. Kartner, X. D. Li, C. Pitris, E. P. Ippen and J. G. Fujimoto, "Spectroscopic optical coherence tomography," Opt. Lett. **25,** 111-113 (2000).
5. R. Leitgeb, M. Wojtkowski, A. Kowalczyk, C. K. Hitzenberger, M. Sticker and A. F. Fercher, "Spectral measurement of absorption by spectroscopic frequency-domain optical coherence tomography," Opt. Lett. **25,** 820-822 (2000).
6. D. J. Faber, E. G. Mik, M. C. G. Aalders and T. G. van Leeuwen, "Light absorption of (oxy-) hemoglobin assessed by spectroscopic optical coherence tomography," Opt. Lett. **28,** 1436-1438 (2003).
7. C. Xu, J. Ye, D. L. Marks and S. A. Boppart, "Near-infrared dyes as contrast-enhancing agents for spectroscopic optical coherence tomography," Opt. Lett. **29,** (2004).
8. B. Hermann, K. Bizheva, A. Unterhuber, B. Povazay, H. Sattmann, L. Schmetterer, A. F. Fercher and W. Drexler, "Precision of extracting absorption profiles from weakly scattering media with spectroscopic time-domain optical coherence tomography," Opt. Express **12,** 1677-1688 (2004).
9. K. D. Rao, M. A. Choma, S. Yazdanfar, A. M. Rollins and J. A. Izatt, "Molecular contrast in optical coherence tomography by use of a pump-probe technique," Opt. Lett. **28,** 340-342 (2003).
10. C. Yang, M. A. Choma, L. E. Lamb, J. D. Simon and J. A. Izatt, "Protein-based molecular contrast optical coherence tomography with phytochrome as the contrast agent," Opt. Lett. **29,** 1396-1398 (2004).
11. M. Born and E. Wolf, *Principles of optics* (Cambridge University Press, Cambridge, 1999).
12. C. Yang, M. A. Choma, J. D. Simon and J. A. Izatt. "Spectral triangulations molecular contrast OCT with indocyanine green as contrast agent." Optical Society of American Biomedical Optics Topical Meetings, Miami, FL, April 14-17, 2004, Paper SB3.
13. C. Xu and S. A. Boppart. "Comparative performance analysis of time-frequency distributions for spectroscopic optical coherence tomography." Optical Society of American Biomedical Optics Topical Meetings, Miami, FL, April 14-17, 2004, Paper FH9.

#4965 - $15.00 US Received 2 August 2004; revised 16 September 2004; accepted 21 September 2004

14. J. M. Schmitt, S. H. Xiang and K. M. Yung, "Differential absorption imaging with optical coherence tomography," J. Opt. Soc. Am. A **15,** 2288-2296 (1998).
15. D. L. Marks, A. L. Oldenburg, J. J. Reynolds and S. A. Boppart, "Digital algorithms for dispersion correction in optical coherence tomography for homogeneous and stratified media," Appl. Opt. **42,** 204-217 (2003).

1. Introduction

Optical coherence tomography (OCT) has been developed to not only image the structure from a sample, but also functional information [1-3]. One functional OCT imaging modality is spectroscopic OCT (SOCT), where spatially-resolved spectroscopic information is extracted [4,5]. SOCT has many biomedical applications, such as qualitative contrast enhancement or quantitative spectral-profile extraction [6-10]. A potentially powerful application of SOCT is to analyze the absorption profiles of native or foreign chromophores embedded in turbid media such as biological tissues. However, there are two mechanisms for the modification of the light spectrum in tissue: scattering and absorption. Typical SOCT measurements are not able to differentiate between these two mechanisms. Most of the pioneering studies using SOCT have only considered spectral modification by absorption, assuming negligible contributions from scattering. This is an unrealistic case in that most biological tissues are turbid, where scattering loss can be orders of magnitude larger than absorption loss. When appropriately chosen absorption dyes are used as spectral contrast agents, the scattering loss is still non-negligible because the dye concentrations used in biological tissues can not be arbitrarily high. In fact, the optimal dye concentrations should be high enough to introduce sufficient spectral contrast but low enough such that the SOCT imaging penetration depth is not severely affected. This optimization usually requires that the absorption loss and scattering loss be within the same order of magnitude. In any case, it is difficult to separately extract absorption profiles and scattering profiles quantitatively because both scatterers and absorbers can arbitrarily modify the spectrum of back-reflected light [11]. However, the spectra of the dominating absorbers in a sample may be known *a priori*, such as when highly absorbing near-infrared (NIR) dyes are used. In addition, the dyes can be chosen such that the dye absorption spectra are very different from the scattering spectra of the tissue. These two pieces of prior information can make separation of absorption from scattering possible.

In a recent proceeding, Yang *et al*. proposed a method for eliminating first-order wavelength-dependent contributions from scattering by three-point spectral triangulation using three narrow-band sources centered at 760 nm, 795 nm and 830 nm, and a differential absorption method to retrieve the depth-resolved location of differential absorption change [12]. In this work, we consider using a single broadband source for quantitative, depth-resolved SOCT. Using a single board band source permits analysis of spectral modification over a broad wavelength range in a single experiment. With the help of time-frequency analysis, the use of broadband sources is equivalent to using multiple narrow-band sources simultaneously. The tradeoff between spatial resolution and spectral resolution can be optimized after data collection, offering both better precision and flexibility [13]. In addition, this approach offers many other advantages, typically permitting better spatial localization of the absorbing object, reducing the complexity of the instruments, and eliminating the artifacts resulting from sample movement and the necessity of registering multiple images. In this paper we propose a new algorithm for differentiating the contributions from absorption and scattering in SOCT using a single broadband laser for the case where NIR dyes are used. This method utilizes time-frequency analysis and a least-square fitting algorithm. The proposed algorithm was tested using both single-layer and multi-layer tissue phantoms. Theoretical and simulated noise analysis is also included.

#4965 - $15.00 US Received 2 August 2004; revised 16 September 2004; accepted 21 September 2004

2. A Model of SOCT Signals

OCT measures the interference fringes generated between beams reflected from a reference mirror and backscattered from scatterers in a sample. Because biological or material samples have depth-varying distributions of absorption and scattering spectra, backscatter from different depth in a sample will have different spectra. For the case of only one strong scatter within the coherence length, the interferometric signal $I(\lambda, z)$ collected from a given depth z can be expressed as the multiplication of source spectrum $S(\lambda)$ and the modulation effect which includes the contributions from spectral backscattering profile $H_r(\lambda, z)$, the lumped spectral modification $H_m(\lambda, z)$ by media before that scatter, and the total spectral modification $H_s(\lambda, z)$ by optical components in the system, such as the beamsplitter, along the optical paths [6,14], i.e.,

$$I(\lambda, z) = S(\lambda) H_r(\lambda, z) H_m(\lambda, z) H_s(\lambda, z). \tag{1}$$

Usually $S(\lambda)$ and $H_s(\lambda, z)$ are stationary and known *a priori*. Therefore measuring $I(\lambda, z)$ offers the opportunity to study the material properties in the sample. For the cases of multiple scatterers within a coherence length, in general the resulting $I(\lambda, z)$ has spectral modulation due to interference of signals from neighboring scatterers. However, this modulation is random due to the random spacing between the scatterers. Therefore, un-modulated spectra can be recovered with high accuracy if sufficient compounding and averaging are applied.

The spectral modification $H_m(\lambda, z)$ by media has both scattering and absorption contributions. In most cases, they follow Beer's law:

$$H_m(\lambda, z) = \exp\left\{-2\int_0^z [\mu_a(\lambda, z') + \mu_s(\lambda, z')]\, dz'\right\}. \tag{2}$$

Here, $\mu_a(\lambda, z)$ and $\mu_s(\lambda, z)$ are wavelength-dependent and spatially-varying absorption coefficients and scattering coefficients of the imaged media, respectively. Assuming the sample is composed of collections of small scatterers of similar sizes and random positions, $H_r(\lambda, z)$ can be approximated by a separable function in λ and z. Disregarding the dispersion and chromatic aberrations in the optical system, $H_s(\lambda, z)$ is also a separable function in λ and z:

$$\begin{aligned} H_r(\lambda, z) &= H_r(\lambda) H_r(z), \\ H_s(\lambda, z) &= H_s(\lambda) H_s(z). \end{aligned} \tag{3}$$

Substituting Eq. (2) and (3) into Eq. (1), we get:

$$I(\lambda, z) = S(\lambda) H_s(\lambda) H_r(\lambda) R(z) \exp\left[-2\int_0^z \mu_a(\lambda, z') + \mu_s(\lambda, z')\, dz'\right], \tag{4}$$

where $R(z) = H_r(z) H_s(z)$.

At $z = 0$, we have:

$$I(\lambda, z = 0) = S(\lambda) H_r(\lambda) H_s(\lambda) R(z = 0). \tag{5}$$

Therefore, the wavelength-dependent factors $S(\lambda)$, $H_r(\lambda)$ and $H_s(\lambda)$ can be eliminated by:

$$I'(\lambda, z) \triangleq I(\lambda, z) / I(\lambda, z = 0) = R'(z) \exp\left\{-2\int_0^z [\mu_a(\lambda, z') + \mu_s(\lambda, z')]\, dz'\right\}. \tag{6}$$

Because the same NIR dye of high absorptivity is used, the absorption coefficient at certain depths depends only on the absorber concentration present at that depth. Assuming the scatterers have similar spectral loss along the sample depth, for the first-order approximation, both $\mu_a(\lambda, z)$ and $\mu_s(\lambda, z)$ are separable functions in λ and z, i.e.,

#4965 - $15.00 US Received 2 August 2004; revised 16 September 2004; accepted 21 September 2004

$$\begin{aligned} \mu_a(\lambda, z) &= \varepsilon_a(\lambda) f_a(z), \\ \mu_s(\lambda, z) &= \varepsilon_s(\lambda) f_s(z), \end{aligned} \tag{7}$$

where $f_a(z)$ represents the absorber concentration and $f_s(z)$ represents the scatterer concentration at a particular depth z. The functions $\varepsilon_a(\lambda)$ and $\varepsilon_s(\lambda)$ represent the absorption and scattering per unit concentration and per unit pathlength. They can be measured by a laboratory spectrometer or by integrating spheres. Then, the exponent term in Eq. (6) can be rewritten as:

$$-2\int_0^z [\mu_a(\lambda, z') + \mu_s(\lambda, z')]\, dz' = -2\left[\varepsilon_a(\lambda)\int_0^z f_a(z')\, dz' + \varepsilon_s(\lambda)\int_0^z f_s(z')\, dz'\right]. \tag{8}$$

Substituting Eq. (8) into Eq. (6) and taking the logarithm to both sides, we obtain:

$$\begin{aligned} Y(\lambda, z) &\triangleq \log\left[I'(\lambda, z)\right] \\ &= \log R'(z) - 2\left[\varepsilon_a(\lambda)\int_0^z f_a(z')\, dz' + \varepsilon_s(\lambda)\int_0^z f_s(z')\, dz'\right] \\ &= -\varepsilon_a(\lambda)F_a(z) - \varepsilon_s(\lambda)F_s(z) + C(z). \end{aligned} \tag{9}$$

Here, for simplification we define:

$$F_a(z) \triangleq 2\int_0^z f_a(z')\, dz', \quad F_s(z) \triangleq 2\int_0^z f_s(z')\, dz', \quad C(z) \triangleq \log R'(z). \tag{10}$$

Notice that $F_a(z)$, $F_s(z)$, and $C(z)$ are wavelength independent functions that we want to find. $Y(\lambda, z)$ can be obtained by time-frequency analysis of the OCT signals.

3. Solving absorption and scattering profiles using least-squares method

Because of the presence of noise and other non-ideal conditions, Eq. (9) typically can only be solved with some optimality criteria. Weighted minimal-mean-square-error (MMSE) optimization is used because it is unbiased and has minimum-variance properties. To do this, the estimation error variable is defined by:

$$E(z) = \int_{\lambda_1}^{\lambda_2} [-F_a(z)\varepsilon_a(\lambda) - F_s(z)\varepsilon_s(\lambda) + C(z) - Y(\lambda, z)]^2\, W(\lambda)\, d\lambda\,, \tag{11}$$

where $[\lambda_1, \lambda_2]$ represents the laser spectral range. We can choose the weighting function $W(\lambda)$ such that more accurate data (such as the spectral information around the central region of the laser spectrum) are emphasized. One possible choice of $W(\lambda)$ is a smoothed function of laser spectral density while another possible choice is a rectangular window corresponding to the FWHM of the laser spectrum.

Taking the derivatives of $E(z)$ in Eq. (11) with respect to $F_a(z)$, $F_s(z)$, and $C(z)$ and setting them equal to zero, the resulting three Eq. can be written in matrix format:

$$\underbrace{\begin{bmatrix} \int_{\lambda_1}^{\lambda_2}\varepsilon_a^2(\lambda)W(\lambda)d\lambda & \int_{\lambda_1}^{\lambda_2}\varepsilon_s(\lambda)\varepsilon_a(\lambda)W(\lambda)d\lambda & \int_{\lambda_1}^{\lambda_2}\varepsilon_a(\lambda)W(\lambda)d\lambda \\ \int_{\lambda_1}^{\lambda_2}\varepsilon_a(\lambda)\varepsilon_s(\lambda)W(\lambda)d\lambda & \int_{\lambda_1}^{\lambda_2}\varepsilon_s^2(\lambda)W(\lambda)d\lambda & \int_{\lambda_1}^{\lambda_2}\varepsilon_s(\lambda)W(\lambda)d\lambda \\ \int_{\lambda_1}^{\lambda_2}\varepsilon_a(\lambda)W(\lambda)d\lambda & \int_{\lambda_1}^{\lambda_2}\varepsilon_s(\lambda)W(\lambda)d\lambda & \int_{\lambda_1}^{\lambda_2}W(\lambda)d\lambda \end{bmatrix}}_{\mathbf{A}} \underbrace{\begin{bmatrix} -F_a(z) \\ -F_s(z) \\ C(z) \end{bmatrix}}_{\mathbf{X}} = \underbrace{\begin{bmatrix} \int_{\lambda_1}^{\lambda_2}Y(\lambda,z)\varepsilon_a(\lambda)W(\lambda)d\lambda \\ \int_{\lambda_1}^{\lambda_2}Y(\lambda,z)\varepsilon_s(\lambda)W(\lambda)d\lambda \\ \int_{\lambda_1}^{\lambda_2}Y(\lambda,z)W(\lambda)d\lambda \end{bmatrix}}_{\mathbf{Y}}. \tag{12}$$

#4965 - $15.00 US Received 2 August 2004; revised 16 September 2004; accepted 21 September 2004

Notice that matrix **A** is independent of depth *z*. After $F_a(z)$, $F_s(z)$, and $C(z)$ are solved by Eq. (12), the absorber concentration profile $f_a(z)$ and the scattering profile $f_s(z)$ can be solved from Eq. (10).

In many cases, the $\varepsilon_s(\lambda)$ can be approximated by a linear function, i.e., $\varepsilon_s(\lambda) = a\lambda + b$, then Eq. (12) can be further simplified as:

$$\begin{bmatrix} \int_{\lambda_1}^{\lambda_2} \varepsilon_a^2 W(\lambda)d\lambda & \int_{\lambda_1}^{\lambda_2} \lambda\varepsilon_a(\lambda)W(\lambda)d\lambda & \int_{\lambda_1}^{\lambda_2} \varepsilon_a(\lambda)W(\lambda)d\lambda \\ \int_{\lambda_1}^{\lambda_2} \lambda\varepsilon_a(\lambda)W(\lambda)d\lambda & \int_{\lambda_1}^{\lambda_2} \lambda^2 W(\lambda)d\lambda & \int_{\lambda_1}^{\lambda_2} \lambda W(\lambda)d\lambda \\ \int_{\lambda_1}^{\lambda_2} \varepsilon_a(\lambda)W(\lambda)d\lambda & \int_{\lambda_1}^{\lambda_2} \lambda W(\lambda)d\lambda & \int_{\lambda_1}^{\lambda_2} W(\lambda)d\lambda \end{bmatrix} \begin{bmatrix} -F_a(z) \\ -aF_s(z) \\ D(z) \end{bmatrix} = \begin{bmatrix} \int_{\lambda_1}^{\lambda_2} Y(\lambda,z)\varepsilon_a(\lambda)W(\lambda)d\lambda \\ \int_{\lambda_1}^{\lambda_2} \lambda Y(\lambda,z)W(\lambda)d\lambda \\ \int_{\lambda_1}^{\lambda_2} Y(\lambda,z)W(\lambda)d\lambda \end{bmatrix}, \tag{13}$$

where $D(z) = C(z) - bF_s(z)$.

Equation (13) is useful when the exact $\varepsilon_s(\lambda)$ is difficult to measure or when $\varepsilon_s(\lambda)$ virtually has no wavelength dependence such that it can not be differentiated from the $C(z)$ term. Eq. (13) is also useful when we are only interested in retrieving the absorber concentration profile, for example, when NIR dyes are used for contrast-enhancement experiments. $C(z)$ in Eq. (12) and $D(z)$ in Eq. (13) are not of interest because $R(z)$ can be estimated from a structural OCT image. In practice, all the above procedures are discretized on *z* and λ.

In SOCT measurements, outlier data may result from some unusual event such as the presence of specular reflections that temporarily exceeds the dynamic range of the signal acquiring system, or due to the presence of rare reflecting points that have large spectral changes such that the assumption of the independence of the scattering spectra with depth is no longer valid. SOCT is also a typically noisy measurement due to various noise sources. Because the matrix on the left side of Eq. (12) or (13) is typically not well-conditioned, data-regularization is helpful for improving the performance. A two-step data regularization procedure is proposed. In the first step, outlier points are removed. The spectral data $Y(\lambda, z)$ corresponding to outliers is usually very different from the expected data in SOCT experiments. After Eq. (12) or (13) is solved, the error function (11) is calculated for all *z* positions. The outliers can be removed by setting appropriate thresholds on the histograms of the error function. The $Y(\lambda, z)$ corresponding to outliers can be replaced by interpolation methods or be excluded from the data sets, depending on the location of outliers. Equation (12) or (13) are then re-solved using updated data.

In the second regularization step, data regularization is performed using a smoothing constraint. Starting from Eq. (12) or Eq. (13):

$$\mathbf{AX} = \mathbf{Y}, \tag{14}$$

the solution to Eq. (14) using the regularization method is:

$$\mathbf{X}_\alpha = \arg\min \left\{ || \mathbf{Y} - \mathbf{AX} ||^2 + \alpha^2 || \mathbf{LX} ||^2 \right\}. \tag{15}$$

The solution to Eq. (15) is:

$$\mathbf{X} = \left(\mathbf{A}^T\mathbf{A} + \alpha^2\mathbf{L}^T\mathbf{L} \right)^{-1} \mathbf{A}^T\mathbf{Y}. \tag{16}$$

Because the absorption/scattering loss is typically a long-range effect, $F_a(z)$ and $F_s(z)$ should be smooth functions of z. The second-order derivatives of $F_a(z)$ and $F_s(z)$ should be very close to zero. Therefore, a Laplacian operator can be chosen for **L**. Notice that the smoothing constraint should not be applied to $C(z)$ or $D(z)$ because they are functions of $R(z)$, which typically is not smooth. Although the sizes of vectorized **A** and **L** matrices are large

#4965 - $15.00 US Received 2 August 2004; revised 16 September 2004; accepted 21 September 2004

(corresponding to the numbers of the depth points), Eq. (16) can be rapidly solved numerically because all matrices are very sparse.

There are typically two experimental scenarios in current SOCT research. The first scenario involves structures that have distinctive layers, such as experiments with cuvettes or layered phantoms. For this scenario, the parameters for time-frequency analysis can be chosen for less time resolution but higher spectral resolution. Far-spaced distinctive z points are taken, and Eq. (12) or Eq. (13) can be solved. The second scenario involves structures that do not have distinctive layers, such as biological tissues or inhomogeneous phantoms without apparent layering. For this scenario, appropriate time-frequency analysis should be chosen with the parameters optimized to meet specific needs. Cumulative absorption $F_a(z)$ and scattering $F_s(z)$ are calculated. The absorber profile $f_a(z)$ and scatterer profile $f_s(z)$ can be retrieved with piece-wise curve-fitting and solving Eq. (10).

4. Noise analysis and simulation

It is instructive to perform noise analysis on the algorithm. Below we only perform a noise analysis using Eq. (12). Noise analysis using Eq. (13) is similar.

In Eq. (12), the variables $\varepsilon_a(\lambda)$ and $Y(\lambda, z)$ are experimentally determined and the windowing function $W(\lambda)$ is chosen. The values for the variable $\varepsilon_a(\lambda)$ are typically measured by a precision spectrometer (error ~ 0.1%), therefore they can be assumed to be highly accurate. $Y(\lambda, z)$, on the other hand, has non-negligible system and experimental errors due to laser spectral drift, laser intensity and spectral noise, presence of chromatic aberrations, dispersion mismatch, angle- and wavelength-dependent back reflection, electronics noise, and errors introduced by data acquisition and time-frequency analysis. Even after extensive averaging, the errors in SOCT measurements still range from 2% to 10%, which have been estimated by analyzing known experimental settings such as measuring the back reflected spectra from upper and lower cuvette interfaces [8].

For simplicity, Eq. (13) can be rewritten as:

$$\mathbf{X} = \mathbf{A}^{-1}\mathbf{Y} . \tag{17}$$

Assuming **A** is exact, we have:

$$\sigma_{x_i}^2 = \sum_{j=1}^{3} b_{ij}^2 \sigma_{y_j}^2 , \tag{18}$$

where b_{ij} are the elements of $\mathbf{A}^{-1}$.

Equation (18) shows that the variance of absorption (scattering) profile retrieval is proportional to the variance of the logarithmic of the time-frequency analysis. Because of the matrix inverse operation, exact analytical noise-analysis is complicated. However, Monte-Carlo simulations can be used to determine the effect of noise contributions. The simulated $I(\lambda, z)$ is constructed based on Eq. (4) using the measured laser spectrum, the dye absorption coefficients, and the scattering coefficients from a real sample containing microbeads (refer to the later experimental section for details). The sample has a $\mu_{a,800nm}$ = 0.5 mm^{-1} and a $\mu_{s,800nm}$ = 0.5 mm^{-1}. R(z) was chosen to be a uniformly-distributed random vector with values between [0.5, 1.5]. The wavelength range was set between 700 nm and 900 nm and the maximum sample depth was set as 1 mm. White Gaussian noise of specified SNR was added to $I(\lambda, z)$. The windowing function was chosen to be the laser source spectrum. Figure 1 shows the effect of noisy time-frequency analysis on the accuracy of the final dye concentration retrieval. The standard deviations for 100 runs at different SNRs are measured as a means of quantifying the accuracy and repeatability of the absorption retrieval.

#4965 - $15.00 US Received 2 August 2004; revised 16 September 2004; accepted 21 September 2004

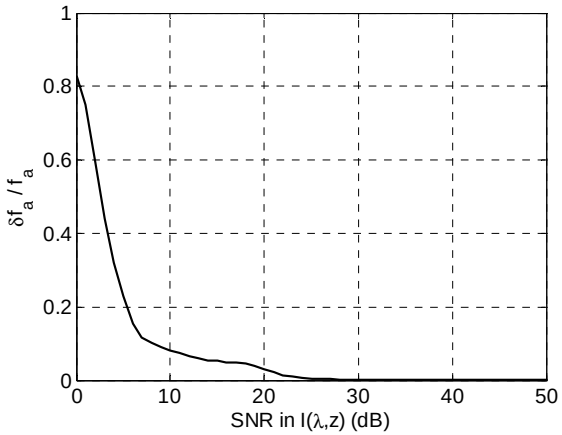

Fig. 1. Errors in retrieved absorption f_a as a function of SNR in SOCT $I(\lambda, z)$.

Figure 1 shows the errors percentage (as quantified by $\delta f_a/f_a$, or standard deviation over the mean) as a function of SNR in the time-frequency analysis of the SOCT signal $I(\lambda, z)$. From Fig. 1, it can be seen that the error increases with worsening SNR. In order to have error percentage smaller than 5%, the time-frequency analysis from the SOCT signals should have a SNR larger than 14dB for this case.

5. Experiments

For the purpose of this study, a fiber-based time-domain OCT system with a broad bandwidth Ti:Al_2O_3 laser source was used (KM Labs, λ_c = 810nm, $\Delta\lambda$ = 130 nm, P_{out} = 300 mW). Dispersion and polarization were matched in the interferometer arms. A thin lens with a 40 mm focal length was chosen to focus the sample-arm beam and to minimize the effect of chromatic aberrations and dispersion. A precision linear optical scanner was used to scan the reference arm. Non-linearities in the reference scanning rate were accounted for by acquiring a reference fringe pattern using a laser diode (λ_c = 776 nm, $\Delta\lambda$ = 1 nm), followed by the application of a data-correction algorithm. The OCT system provided 4 μm axial and 26 μm lateral resolution with a 3.2 mm depth of focus in air. The system SNR was 110 dB with 11 mW of sample power. The typical power incident on the sample for these studies was 10 mW. The interfering signal and reference light was detected using an auto-balancing detector (Model 2007, New Focus, Inc.). The signal was amplified and anti-aliasing low-pass filtered by a custom-made analog circuit. A high-speed (5 Msamples/s, 12-bit) A/D converter (NI-PCI-6110, National Instruments) was used to acquire interferometric fringe data.

Axial scans comprising the interferometric signals were sampled at 100,000 data points, and at 512 transverse positions to form two-dimensional images. Collected data were analyzed using Matlab. First, the data were demodulated and down-sampled to baseband to obtain analytical signals such that only the frequency bands corresponding to laser spectrum remained and were expanded to fill the whole digital frequency band. The down-sampling process not only improved calculation speed in subsequent steps, but also rejected the out-of-band noise. Digital dispersion correction was applied to correct the small dispersion mismatch between the sample arm and the reference arm once hardware path-length matching was performed [15]. Dispersion correction minimized the mismatch in the center region of the sample, corresponding to the span of the axial scans. The down-sampled signals were then analyzed with time-frequency distributions. For studies shown in this paper, the short-time Fourier transform (STFT) with overlapping windows were used for its reliability and flexibility. Gaussian windows with widths corresponding to 10 laser-source coherence lengths were used for distinctive interfaces and 5 laser-source coherence lengths for turbid

#4965 - $15.00 US Received 2 August 2004; revised 16 September 2004; accepted 21 September 2004

media (corresponding to approximate spectral resolutions of 10 nm and 20 nm, respectively). To decrease the possible noise influence and increase the calculation precision, each spectrum frame in the STFT was interpolated to 100 spectral points using a cubic Spline interpolation algorithm. The exact correspondence between the digital frequency from the time-frequency analysis and the laser wavelength was established using a narrow-band laser diode. When the same data analysis method was applied to the interference fringe data obtained using a laser diode, the relationship between the digital frequency F of the analytical signal and the corresponding light wavelength λ could be calculated by:

$$F = \frac{\lambda_{LD}[F_{LD}(F_{high} - F_{low}) + F_{low}]}{\lambda(F_{high} - F_{low}) + F_{low}} \tag{19}$$

Where λ_{LD} is the laser diode center wavelength. F_{high} and F_{low} correspond to the digital frequency ranges used in the down-sampling step. F_{LD} is the digital frequency obtained from SOCT using a laser diode and a perfect mirror. After data processing, the spectra were averaged over 512 scan lines to reduce noise.

The spectrum of the dye and scattering agents measured with a spectrometer were also interpolated by cubic Spline using Eq. (19). The interpolation first rescaled the wavelength spectra to frequency spectra and then resampled the spectra such that the spectral points have a one-to-one correspondence to the spectral points obtained from time-frequency analysis.

Figure 2 shows the emission spectrum of the Ti:sapphire laser, the dye absorption spectra, and the wavelength region chosen for the weighting function $W(\lambda)$. Because the emission spectrum of the Ti:sapphire laser had a somewhat flattened top with a fast fall-off at each end, a rectangular $W(\lambda)$ corresponding to the FWHM of the laser spectrum was chosen.

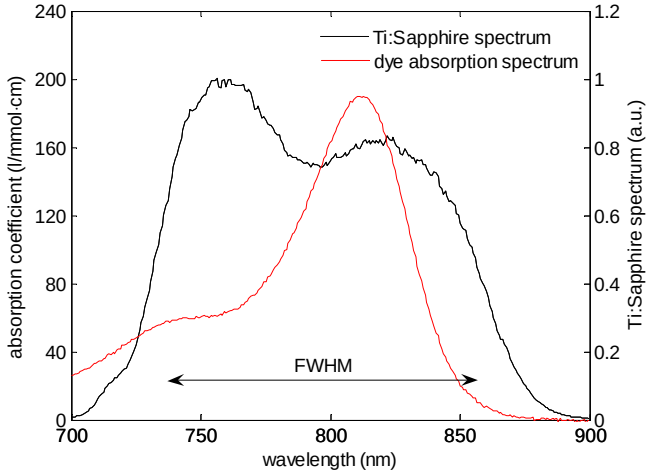

Fig. 2. Emission spectrum of the Ti:Al_2O_3 laser (black curve) and absorption spectrum of dye ADS830WS (red curve). Also shown is the FWHM region used for determining $W(\lambda)$.

Phantoms were made in liquid form rather than in gel form for easy handling and accurate concentration control. A NIR dye (ADS830WS, American Dye Sources) was used for these experiments. This dye offer many advantages over other NIR dyes: the absorption profile of this dye has a sharp peak around 810 nm which is near the center of the emission spectrum of the Titanium:sapphire laser. Unlike many other water-soluble NIR dyes, this dye follows Beer's absorption law up to very high concentrations in a water-methanol solution (water content: 10%). The photo-bleaching effect, manifested by numerous other NIR dyes, is absent in this dye. Experimentally, the absorption profile of this dye does not change over 20 minutes under a focused 10mW laser beam. Silica microbeads (0.16 μm diameter, Bangs

#4965 - $15.00 US Received 2 August 2004; revised 16 September 2004; accepted 21 September 2004

Laboratories, Inc.) were used as scattering agents. Appropriate amounts of dye and microbeads were mixed to give the desired absorption and scattering properties. The absorption properties of dye–only and microbead-only solutions at different concentrations were measured with a spectrometer (Ocean Optics, USB2000).

The choice of appropriate time-frequency analysis is important for the performance of SOCT analysis and should be chosen based on specific applications [13]. For the short-time Fourier transform (STFT) with overlapping Gaussian windows as used in this paper, the window size is a critical parameter. The spatial resolution directly corresponds to the window size. Choosing a longer window provides a better dye concentration estimate, but worsens the spatial resolution. The spectral resolution ($\delta\lambda$) using the STFT can be roughly estimated by

$$\delta\lambda = \frac{\lambda_c^2}{2\, l_{STFT}}, \tag{20}$$

where l_{STFT} is the short window length and λ_c is the center wavelength of the laser spectrum. The exact spectral resolution can be measured by performing an analysis of SOCT signals obtained from a narrow-band laser diode source and a mirror as the sample. A general guideline for choosing the window size is that the window size should be large enough such that absorption features of the dye are distinguishable with sufficient accuracy but not overly degrade the spatial resolution.

6. Results

The SOCT system performance was first checked for overall performance according to the procedures outlined by Hermann et. al. [8]. Within the FWHM of the laser emission spectrum (740nm - 860nm) arriving at the sample, the acquired SOCT spectrum from a mirror after averaging 512 A-scans has a standard deviation well below 2%. To further evaluate the performance of the SOCT system, the absorption profile of a pure dye solution was measured by analyzing the SOCT spectra from the upper and lower liquid/glass interfaces of a 1 mm-thick cuvette filled with dye of peak absorption coefficient of 0.5 mm^{-1} according to procedures outlined by Hermann *et al.* [8]. The precision of the retrieved spectral profile between 750nm and 850 nm is within 5% from what was measured by the spectrometer.

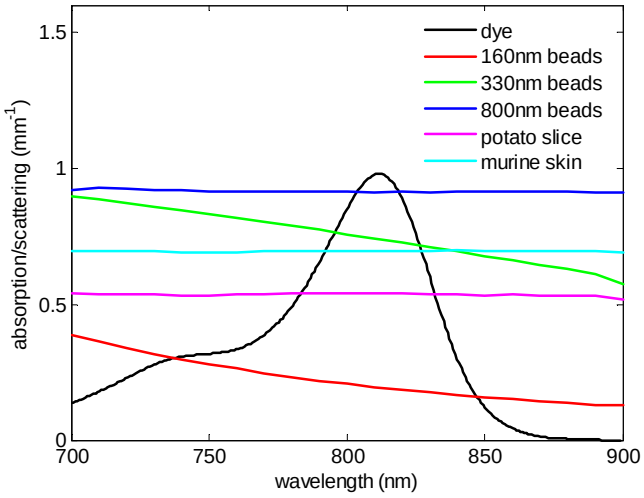

Fig. 3. Absorption/scattering attenuation loss due to various absorbers/scatterers as measured by a spectrometer: 40 μM ADS830WS NIR dye solution, 1% 160 nm silica microbead solution, 0.5% 330 nm silica microbead solution, and 0.5 % 800 nm silica microbead solution, potato slice, and murine skin.

#4965 - $15.00 US Received 2 August 2004; revised 16 September 2004; accepted 21 September 2004

To validate the assumption that most scattering specimens have a linear scattering profile within the laser spectrum, several representative specimens were measured with a spectrometer. The specimens chosen included silica-microsphere solutions with bead-sizes of 0.16, 0.33 and 0.8 μm, thin slices of potato, and murine skin. All specimens examined showed that scattering loss was linearly-dependent on wavelength with correlation coefficients ranging from 0.987 to 0.999 (Fig. 3). In comparison, the correlation coefficient for the dye absorption profile was measured at 0.202. Therefore, there exists significant difference between the dye absorption profile and the scattering attenuation profiles. To check if the assumption that scattering coefficients and absorption coefficients are additive, we mixed solutions with various dye concentrations and various silica-microsphere concentrations. The total spectral loss was determined by a spectrometer and compared to the sum of the spectral loss of individual components. The results showed that the absorption and scattering coefficients were indeed additive with an error below 2%, which was most likely due to errors in sample preparation.

To test the effectiveness of the algorithm for distinct interfaces, solutions of both dye and microbeads were made. The concentrations of dye and microbeads were adjusted such that they both have approximately the same 0.25 mm^{-1} attenuation at 800 nm. These solutions were placed into 1-mm-thick glass cuvettes and imaged with SOCT. The cuvette direction was adjusted such that light reflecting from glass/liquid interfaces went straight back to the fiber collimator. The maximized specular reflections collected by the detector from the glass/liquid and liquid/glass interfaces were much greater (at least 40 times larger) than the light scattered from the microbeads. Neutral density filters were used to avoid saturation of the detector. The interference data from light scattered back from the top glass/dye interface and the bottom dye/glass interface were recorded and analyzed using a Fourier transform window size of 10 coherence lengths to extract the SOCT spectra. Figure 4 shows the attenuation spectra extracted with SOCT from the solutions, and their respective separation results using prior spectral measurement of $\varepsilon_a(\lambda)$ and $\varepsilon_s(\lambda)$ obtained with a spectrometer. The algorithm successfully separated the absorption and scattering profiles with a mean error percentage of 4% and a maximum error percentage of 11% from 750 nm to 850 nm.

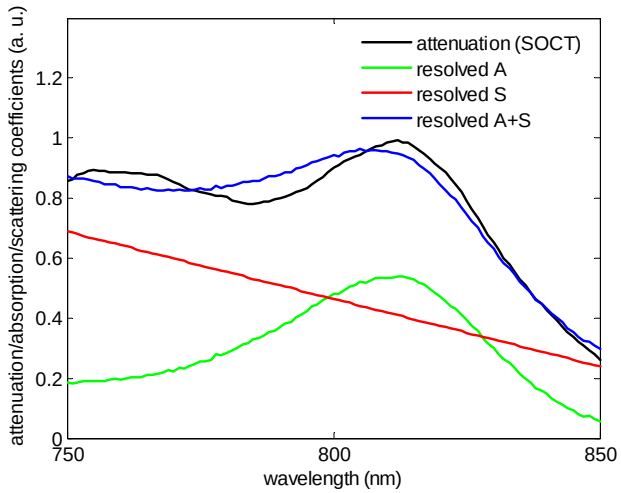

Fig. 4. Separation of absorption and scattering losses from distinctive interfaces: total attenuation profile measured by SOCT (black curve), resolved absorption profile by the separation algorithm (green curve), resolved scattering profile by the separation algorithm (red curve), the sum of the resolved absorption profile and the resolved scattering profile (blue curve).

#4965 - $15.00 US Received 2 August 2004; revised 16 September 2004; accepted 21 September 2004

To evaluate the ability of SOCT to resolve different dye concentrations in the presence of scatterers, a series of 5 samples with both dye and microbeads were constructed. The dye concentrations were chosen to cause peak absorption coefficients at 0.1, 0.2, 0.3, 0.4 and 0.5 mm^{-1}. The microbead concentration was chosen to give a scattering coefficient of 0.25 mm^{-1} at 800 nm for all 5 samples. To evaluate the ability of SOCT to resolve different scatterer concentrations in the presence of dyes, another series of 5 samples were constructed with the same concentration of dye (peak absorption at 0.25 mm^{-1}) but different microbeads concentrations such that the scattering coefficients at 800 nm were 0.1, 0.2, 0.3, 0.4 and 0.5 mm^{-1}. The solutions were placed inside a 1 mm-pathlength cuvette and imaged with SOCT. The cuvette was tilted such that specular reflections off the interfaces were off axis and the light collected at the detector from the interfaces was small.

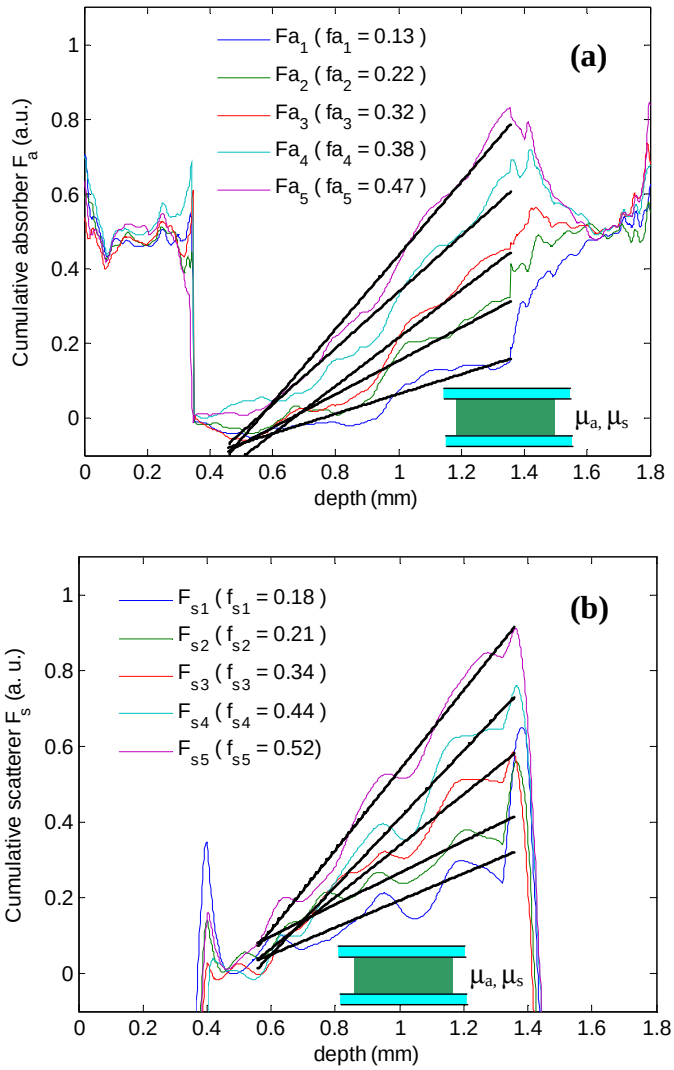

Fig. 5. Resolved absorber and scatterer concentrations in turbid media. (a) Resolved cumulative dye concentrations from solutions with different dye concentrations but the same microbead concentration. (b) Resolved cumulative microbead concentrations from solutions with different microbead concentrations but the same dye concentration. The smooth lines represent the least-squares-fitted model of Eq. (10). The resolved concentrations retrieved from the slopes of the fitted lines are shown as well. The insets show the diagrams of the samples.

#4965 - $15.00 US Received 2 August 2004; revised 16 September 2004; accepted 21 September 2004

Figure 5 shows the experimentally-retrieved cumulative absorber and scatterer concentration ($F_a(z)$ and $F_s(z)$) along with their respective linear-regression curve-fitting from the 10 samples obtained by solving Eq. (12) and Eq. (10). Along the axial scan depth, the cumulative absorption/scattering curves can be roughly divided into three regions: the glass region, top media region, and bulk media region. In the glass region, the signals were mostly noise because there was virtually no scatterer in the upper and bottom glass walls of the cuvette. The top media region ranges from the top glass/liquid interface to 0.1 mm into the sample. The SOCT data from this region was used to obtain the reference spectrum $I(\lambda, z = 0)$ used in Eq. (5). Hence $F_a(z)$ and $F_s(z)$ are mostly flat in this region. The bulk media region ranges from about 0.1 mm into the media to the bottom liquid/glass interface. This region was used to retrieve the absorber/scatterer concentrations. From Fig. 5, the algorithm

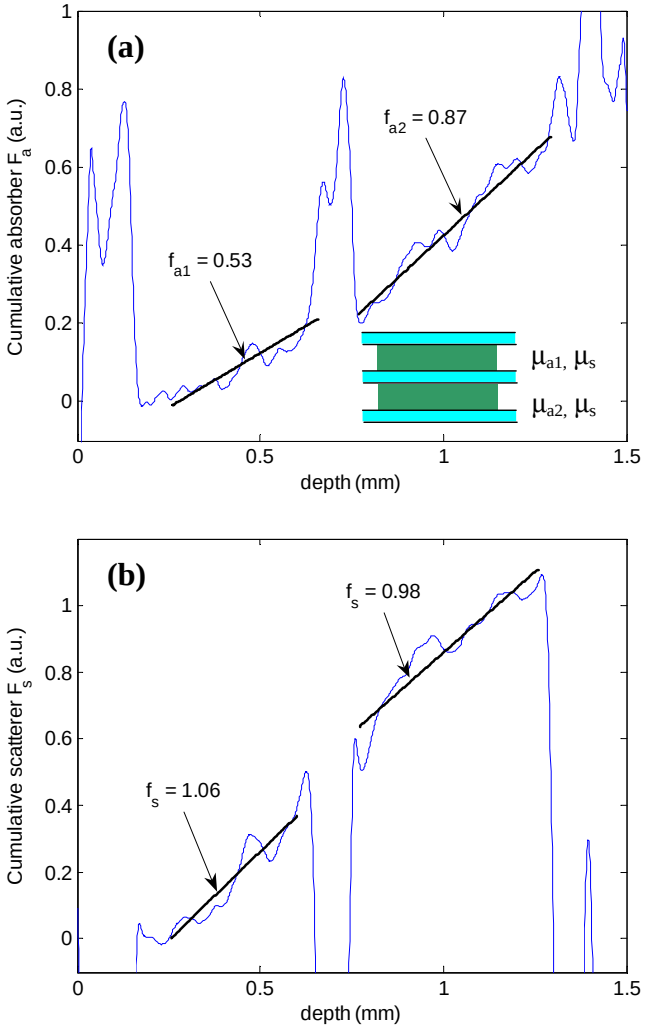

Fig. 6. Resolved absorber and scatter concentrations in a turbid multi-layer phantom. (a) Resolved cumulative dye concentration. (b) Resolved cumulative microbead concentration. The lines represent the least-squares-fitted model of Eq. (10). The resolved concentrations retrieved from the slopes of the fitted lines are also shown. The inset in (a) shows the diagram of the samples.

#4965 - $15.00 US Received 2 August 2004; revised 16 September 2004; accepted 21 September 2004

successfully resolved different absorber (scatterer) concentrations despite the presence of scatterers (absorbers). The errors associated with the resolved scatterer concentration were larger than the error associated with the resolved absorber concentration. This error discrepancy might be due to the presence of multiple scatterings that the algorithm is not able to resolve. The errors of different samples have similar dependency on the depth, indicating the presence of system errors due to non-idealty in OCT system and signal processing algorithms.

To evaluate the ability of the algorithm to retrieve absorber concentrations between regions in the sample with different absorption and scattering properties, measurements and analyses were performed in multi-layer phantoms. The phantoms were constructed with No. 0 coverslips and precision-made self-adhesive silicone spacers (Bioscience Tools, Inc.). The coverslips had a thickness around 100 μm and the thickness of the chambers formed by the silicone spacers was around 500 μm. The top layer had a peak absorption of 0.2 mm^{-1}, and an average scattering loss of 0.2 mm^{-1}, while the bottom layer had a peak absorption of 0.4 mm^{-1}, and an average scattering loss of 0.2 mm^{-1}. Figure 6 shows the cumulative absorber and scatterer concentrations extracted from the two-layer samples, along with their respective linear-regression curve-fitting obtained by solving Eq. (13) and Eq. (10). Similarly, the cumulative absorption/scattering curves can also roughly be divided into three regions: glass region, top media region and bulk media region. The top media region ranges from the top glass/liquid interface to 0.1 mm into the sample in the top layer. As seen from Fig. 6, the algorithm successfully resolved the relative absorber and scatterer concentrations with reasonable accuracy along different depths in the same sample.

The results presented here demonstrate that this algorithm is capable of separately measuring the absorption and scattering contributions of the final SOCT time-frequency analysis in a spatially-resolved way. Although all experimental demonstrations in this paper were done with a time-domain OCT system, the algorithm is also applicable to spectral-domain OCT imaging. The prerequisites for this algorithm are that the absorption spectra of dominating absorber must be known *a priori*, and the scattering spectra of scatterers within the sample are relatively uniform. However, for many important applications, these prerequisites can be met. Absorbing contrast agents, such as NIR dyes, have known absorption profiles and can be site-specifically added as labels in biological tissue. Our algorithm can be used to quantitatively map out the spatial distribution of such contrast agents. In natural biological tissue, strong absorbers such as blood or melanin have well-characterized absorption profiles that if not known, can typically be measured using integrating spheres. However, because there are likely to be multiple absorbers co-existing in the tissue, precise characterization of the absorption profiles will require even more sophisticated multi-component spectral analysis methods.

7. Conclusion

In conclusion, we have developed a least-square fitting algorithm for separating the absorption and scattering profiles in SOCT when a NIR dye is used. This algorithm is theoretically optimal because it is unbiased and has minimum-variance properties. This algorithm was demonstrated using a broad-band laser source together with time-frequency analysis of the SOCT signals. These results are very promising for the development of SOCT contrast agents, especially considering the recent emphasis on developing NIR dyes and their rapidly-expanding application areas.

Acknowledgments

We gratefully acknowledge the collaborative insight and direction from Prof. Alex Wei at Purdue University, the scientific contributions from Tyler Ralston and Amy Oldenburg, and the technical assistance from Ron Stack at the Beckman Institute for Advanced Science and Technology, University of Illinois Urbana-Champaign. This work was supported in part by

NASA and the National Cancer Institute (NAS2-02057) and the National Institutes of Health (NIBIB) (1 R01 EB001777-01).

#4965 - $15.00 US Received 2 August 2004; revised 16 September 2004; accepted 21 September 2004